Egyptian Journal of Chemistry

http://ejchem.journals.ekb.eg/

Synthesis, characterization, and heavy metal removal efficiency of zinc sulfide nanoparticles (zsn's)

Doaa A. Ali[a], Emad E. El-Katori [b,*], A. M. Nagiub[a]

[a]Chemistry Department, Faculty of Science, Al-Azhar University (Assiut), Egypt
[b]Department of Chemistry, Faculty of Science, New Valley University, El-Kharja 72511, Egypt
*e-mail: emad_992002@yahoo.com; emad_elkatori@sci.nvu.edu.eg
Tel: 00201023318210   Fax: 0020927925393

Abstract

In this study, our goal was to create ZnS nanoparticles (ZSN's) and use them to remove different heavy metals, such as iron and phosphate, from aqueous solutions. A sol-gel process was used to create ZnS nanoparticles, which is a quick and effective way to produce vast quantities of nanoscale ZnS. XRD, IR, UV-vis DRS, BET, and TEM techniques were used to analyze the surface properties and material structure of ZnS. The adsorption capacity of the ZnS (ZSN's) was assessed by several experiments. To determine the ideal conditions for iron and phosphate removal, the pH solution effects (2–10), contact time (10–180 min), adsorbent dosage (20–200 mg), and beginning iron and phosphate concentration (10–200 mg/l) on the capacity of adsorption were examined. Results indicated a high iron and phosphate removal at pH 10 after 120 min with an adsorbent dosage of 10 mg. Iron and phosphate followed the Langmuir isotherm in their adsorption, with maximal adsorption capacities of 23.3 and 31.3 mg/g, respectively. Kinetics data were expressed in a pseudo-second-order mode with R^2 values of 0.96 and 0.99 for iron and phosphate. The real samples showed a removal efficiency of 92.2% for iron and 86.5% for phosphate.

Keywords: Zinc sulfide (ZSN's); Iron; Phosphate; Nanoparticles; Adsorption.

1. Introduction

The release of heavy metals into the environment due to industrialization and urbanization poses significant challenges globally. Heavy metal ions are toxic and non-biodegradable, which can negatively impact the environment. The presence of these pollutants in water systems is a major concern [1]. Heavy metal pollutants in water are very stable and difficult to remove. They tend to be absorbed by suspended particles and underwater silt, leading to long-term contamination of water bodies [2]. Iron is one of the heavy metals that can be found in the environment. It mostly exists as ferrous Fe (II), which is a soluble reduced divalent form. This form can dissolve minerals from soil layers when it meets rain, surface runoff, or wastewater. Moreover, iron can also be present in groundwater due to corrosion of steel and cast-iron pipelines or the use of iron coagulants [3]. Iron in water can cause high turbidity, staining, and deposition in water distribution systems, as well as foul smell and dark color [4]. The accumulation of

iron has harmful effects on the human body [5]. The maximum allowed amount of iron in drinking water is 0.3 mg/l, as higher amounts are unsuitable for use in industry and home applications [6]. Excessive phosphorous discharge into water bodies has caused eutrophication to become a global environmental concern [7]. Wastewater contains phosphorus in various forms, including phosphate (H2PO4-, HPO42-, and PO43-), polyphosphate, and organic phosphate, and it is often responsible for harmful algal growth. [8]. When there is an excessive number of algae in a body of water that has an excess of nutrients, it can lead to a depletion of oxygen in the water. This can cause harm to aquatic life such as fish [9]. Therefore, to prevent this from happening, the United States Environmental Protection Agency recommends that the upper limit for phosphorus in water should be 10 µg/L [10]. Removing iron and phosphate from groundwater and wastewater is crucial for environmental and health reasons. There are several effective methods available for reducing or eliminating the amount of

_____

iron in groundwater, such as ion exchange [11], reverse osmosis [12], chemical precipitation [13], electrolysis [14], adsorption [15] physio-chemical processes [16], chemical precipitation [17], and biological methods [18]. One of the most used methods for removing iron and phosphate from water is through adsorption. This technique is reliable and efficient, as well as environmentally friendly and cost-effective. Due to its flexibility and high efficacy, it has become a popular choice for many industries looking to treat aqueous solutions [19-22]. The potential of nanoparticles in wastewater treatment and environmental cleanup is enormous due to their large surface area, self-assembly potential, high selectivity, reactivity, and catalytic potential [23, 24]. Nanometal sulfides, including zinc sulfide (ZnS), are gaining interest due to their low cost, easy manufacturing, and ion exchange capacity [25]. Zinc sulfide (ZnS) is a material with versatile properties that make it suitable for a wide range of applications, including electroluminescence [26], lasers [27], light-emitting diodes (LEDs) [28], and bio-devices [29], as shown by several studies. In this study, ZnS nanoparticles were obtained through the sol-gel method with Triethanolamine as a new caping and templating agent and used as adsorbents for iron and phosphate in a batch adsorption process. The experiment evaluated several factors, such as adsorbent dosage, initial concentration of iron and phosphate, solution pH, and contact time. The study also calculated and discussed the kinetic and isotherm adsorption process.

2. Experimental:
2.1 Materials
The analytical-grade chemical reagents were all provided by Sigma Aldrich Co. and used without further purification. All the solutions were made with distilled water. The next reagents were applied: Zinc acetate dihydrate [$Zn(CH_3COO)_2.2H_2O$], triethanolamine, sodium sulfide monohydrate ($Na_2S.9H_2O$), ethanol absolute, potassium dihydrogen phosphate (KH_2PO_4), iron (II) sulfate ($FeSO_4.7H_2O$), hydroxylamine $NH_2OH.HCl$, ammonium molybdate ((NH_4)$6Mo_7O_{24}.4H_2O$), ammonium metavanadate (NH_4VO_3), sodium acetate ($NH_4C_2H_3O_2$), and and1,10-phenanthroline monohydrate ($C_{12}H_8N_2$). All the glassware was cleaned with dilute acid. The dried glassware was utilized.

2.2 Fabrication of ZnS nanoparticles (ZSN's)
ZnS nanoparticles were synthesized using the following method: 0.5 M of zinc acetate dehydrate was dissolved in 100 ml of distilled water, and the solution was stirred for about 20 minutes. Next, 50

ml of Triethanolamine (10% v/v) was gradually added to the solution as a templating agent, and the mixture was stirred for an additional 30 minutes. Then, 50 ml of a 0.5 M Na_2S solution was added dropwise to the mixture while stirring continuously for 4 hours. The resulting white sol was aged at ambient temperature for 24 hours to produce a gelatinous phase. The precipitate was filtered and repeatedly washed with ethanol and distilled water to eliminate contaminants. Finally, the product was dried for 8 hours at 80°C in the furnace to obtain a fine powder.

2.3 Material characterization
The structure of the crystalline phase of the prepared sample was characterized by Shimadzu, Japan's X-ray diffraction (XRD-6100) by Cu Kα radiation (λ = 0.154178 nm). The FTIR spectrum that has been performed by Nicolet is 50. UV-Vis diffuse reflectance spectra were recorded using the JASCO spectrometer model V-570. BElSORP max ll equipment is used to determine the various properties of the produced sample from adsorption-desorption isotherms. The manufactured sample's microstructure was examined using transmission electron microscopy (JEM 100CX11).

2.4. Adsorption procedure
In this study, we investigated the use of ZnS (ZSN's) in batch adsorption mode to eliminate iron and phosphate ions from a sample solution. We used two beakers, each containing 50 mg of ZnS (ZSN's) and 50 ml of iron and phosphate solution at a concentration of 10 mg/l. The solutions were then placed on a shaker (250 rpm). We studied the factors that influence the adsorption process, such as contact time (10–180 min), pH of solution (2–10), adsorbent dosage (20–200 mg), and initial concentration of iron and phosphate (10–200 mg/l). After adsorption was complete, we used a centrifuge to separate the adsorbent from the solution. We measured the remaining concentrations of iron and phosphate ions in the solution using a UV-visible spectrophotometer (phenanthroline method for iron and vanadomolybdophosphoric acid colorimetric method for phosphate). We used Equation (1) to calculate the removal efficiency (E%), and Equation (2) to calculate the adsorption capacity at equilibrium (qe):

$$E\% = ((C_0 - C_t)/C_0) \times 100 \qquad (1)$$
$$q_e = ((C_0 - C_t)V)/m \qquad (2)$$

Where the q_e is the equilibrium adsorption capacity (mg g^{-1}), C_0 is the initial concentration of Iron and phosphate before adsorption (mg L^{-1}), C_t is the concentration of Iron and phosphate at time t (mg L$^-$

_____

[1], V is the aqueous solution volume (L), and m is the adsorbent dosage (g).

3. Results and Discussion
3.1 XRD of the synthesized ZnS
The (111), (220), and (311) planes may be seen in the XRD patterns of ZnS NPs, which correspond to the cubic zinc mix phase, JCPDS number 080-0020, illustrated in **Fig. 1**. There were no impurity-related diffraction peaks seen in the sample. The Debye-Scherer equation has been used to determine the diameter of ZnS particles [30]. $D = 0.9\lambda/\beta \cos\theta$, where β is the full width at half maximum (FWHM) of the diffraction peak in radians, θ is Bragg's diffraction angle, and λ is the wavelength for the $K\alpha_1$ component of the copper radiation employed (1.54 Å). The average particle size is about 54 nm.
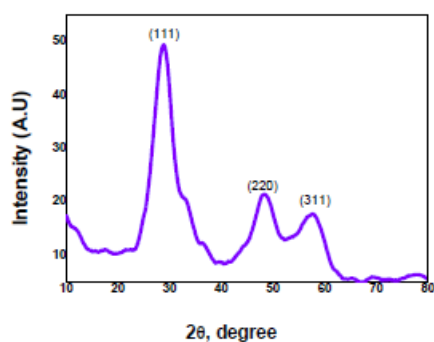

Fig. 1: XRD Spectra of ZnS nanoparticles

3.2 FT-IR spectra
FT-IR spectra of ZnS (ZSN's) are displayed in **Fig. 2.** It reveals many characteristic peaks; the broad absorption band at 3360 cm^{-1} is attributed to the O-H stretching mode of H$_2$O absorbed on the surface of the particles. The two bands observed at 1560 and 1418 cm^{-1} are due to the C=O asymmetric stretching. The peaks appearing at 672, 619, and 478 cm^{-1} are associated with Zn-S vibration and are characteristic of cubic ZnS [31].

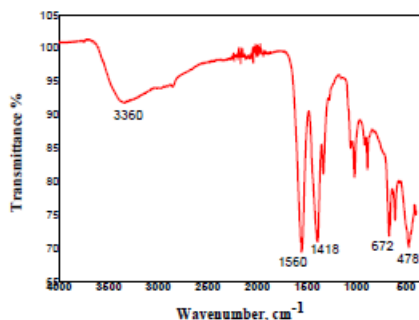
Fig. 2: FT-IR spectra of ZnS nanoparticles

3.3 Optical properties
Fig. 3a shows the absorption spectra of ZnS (ZSN) nanoparticles. The spectra peaks between 250-380

nm, indicating the band gap of the particles. There is no absorption peak in the visible region of 400-800 nm. The Tauc plot can determine the optical band gap of the ZnS nanoparticles using the equation $[(\alpha h\upsilon)n = A(h\upsilon - Eg)]$, where α is the absorption coefficient, $h\upsilon$ is the incident photon energy, A is a constant, and Eg is the band gap energy of the material. The type of transition determines the exponent n, which is 2 for direct transition and 1/2 for indirect transition. The band gap of ZnS NPs was found to be 3.6 eV, as shown in **Fig. 3b**.
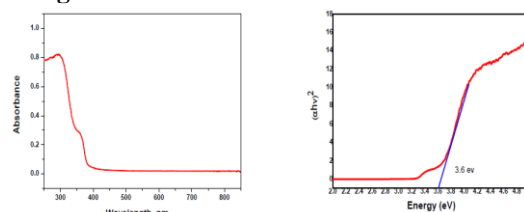

Fig. 3: (a) UV-Vis spectra and (b) Taue plot of ZnS nanoparticles.

3.4 Textural characterization
As shown in **Fig. 4a,** the produced ZnS (ZSN's) exhibits a typical type IV N$_2$ adsorption-desorption combining with H$_3$ hysteresis loop in the P/P0 range of ~0.4–0.98, which is consistent with the mesopore system. The pore-size distribution obtained using the Barrett-Joyner-Halenda (BJH) method indicates a narrow peak centered at 4 nm as shown in **Fig. 4b**. The smaller pore size may derive from the aggregation of ZnS crystals in the porous spherical core. The sharp distribution of mesopores suggests that nanoparticles have uniform internal structures. The BET surface area (S$_{BET}$) and pore volume of ZnS (ZSN's) are about 57 m^2 g^{-1}.and 0.115 cm^3 g^{-1} respectively.

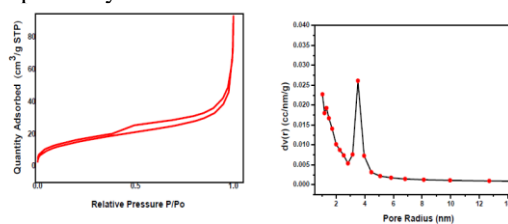Fig. 4: (a) N2 adsorption-desorption isotherms (b) BJH pore size distribution curves of ZnS nanoparticles.

3.5 Transmission Electron Microscope (TEM)
Fig. 5 displays a TEM image of the ZnS nanoparticles and depicts nearly spherical aggregates. The particle size of ZnS is around 60 nm. The size of particles observed in the TEM micrograph agrees with crystallites estimated from the Debye-Sherrer formula.

Fig. 5: TEM images of ZnS nanoparticles (ZSN's).

3.6 Batch Adsorption Study
The iron and phosphate adsorption on ZnS (ZSN's) was examined as a function of contact time, medium pH, ZnS nanoparticle dose, and the initial iron and phosphate ion concentration employed to optimize circumstances. The results are shown in **Figs. 6(a)** through **6(d)**, correspondingly. Understanding the adsorption process is greatly aided by the study of the adsorption rate. The effect of contact time on the adsorption of iron and phosphate was studied at the initial concentration of 10 mg/L (while maintaining pH medium at 6.5 and the adsorbent dose of 50 mg/50 ml) and various adsorption times from 10 to 180 min. The entire adsorption process started with quick adsorption within ten minutes, progressed to a process of the adsorption rate gradually slowing down, and finally reached equilibrium. The equilibrium time of the iron and phosphate solution with an initial concentration of 10 mg L^{-1} was determined to be 120 min, as shown in **Fig. 6a**. The pH of the sample solution is a crucial variable since it may have an impact on the chemical makeup of the analytes as well as the surface characteristics of the adsorbent. [32-34]. **Fig. 6b** shows the impact of pH on the adsorption of iron and phosphate in the range of (2–10) with an initial concentration of 10 mg/l at 120 min. For iron, the results demonstrate that the increase in pH increases the adsorption amount from 6 mg/g at pH 2 to 9.9 mg/g at pH 10. This significant increase might be caused by the precipitation of iron in the form of a Fe^{3+} hydroxide brown precipitate [35]. For phosphate ions, the adsorption amount decreases slightly in the acidic medium, reaching 8.3 mg/g at pH 2, and increasing slightly to 9.2 mg/g at pH 10. One of the crucial factors that significantly influences the adsorption capacity is the amount of adsorbent. The impact of adsorbent dosage was studied with different amounts of ZnS from 20 mg to 200 mg (the initial concentration was 10 mg/l with a procedure time of 120 min) (**Fig. 6c**). It demonstrates that when the dose of ZnS (ZSN's) increased, the amount of adsorption increased from 5 mg/g to 9.95 mg/g for iron ions and increased from 8 mg/g to 9.9 mg/g for

phosphate ions. This increase in the amount of adsorption is due to an increase in the active site of the adsorbent. The ideal concentration of the adsorbent for both ions was determined to be 100 mg. The impact of initial iron and phosphate concentrations on the adsorption capacity is seen in **Fig. 6d** at a dose of 100 mg and an initial concentration of 10 mg/l to 200 mg/l. For iron and phosphate, the adsorption capacity rose noticeably from 9.3 mg g1 to 22 mg g^{-1} and from 8.7 mg g^{-1} to 30 mg g^{-1}, respectively.
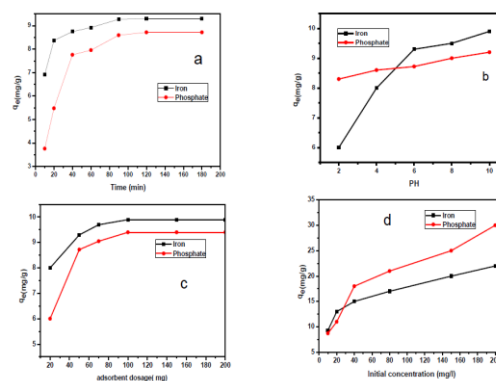

Fig. 6: Effect of time (a) , PH (b) , adsorbent dosage (c) and intial concentration on the iron and phosphate adsorption by ZnS in aqoues solution.

3.2. Kinetics and isotherm analysis
3.2.1 Kinetic studies
To further understand the iron and phosphate ion adsorption processes on ZnS nanoparticles, kinetic studies were conducted to identify the process's rate-limiting phase. When solution species are adsorbed on solid surfaces, we have studied four equation models: pseudo-first-order, pseudo-second-order, intra-particle diffusion, and the Elovich equation. Equation (3) describes kinetics and the linearized form of pseudo-first order [36, 37]. Equation (4) describes the pseudo-second-order expression's linearized form. Equation (5) describes intra-particle diffusion. Equation (6) describes the Elovich equation.

$$ln\ (q_e - q_t) = ln\ q_e - k_1 t \qquad (3)$$

$$\frac{t}{q_t} = \frac{1}{K_2 q_e^2} + \frac{t}{q_e} \qquad (4)$$

Here, q_t and q_e are the amount of solute adsorbed per mass of sorbent (mg g^{-1}) at time (t) and equilibrium (e), respectively. k_1 (min^{-1}) and k_2 (g mg $^{-1}$ min^{-1}) are the equilibrium rate constant of the pseudo-first order and the pseudo-second order kinetics, respectively.

$$q_t = k p_t^{1/2} + C \qquad (5)$$

where, Kp (mg/g·min1/2) is the intraparticle diffusion rate constant and C is the intercept. By drawing qt on

the Y-axis against t (min) on X-axis we can find the slope, intercept, and correlation coefficient:

$$q_t = (1/\beta)\ln(\alpha\beta) + (1/\beta)\ln t \qquad (6)$$

Where q_t symbolizes the adsorption capacity (mg g^{-1}) at time t (min), and α and β indicate the rate of chemisorption (mg g^{-1} min^{-1}) at zero coverage and the desorption constant (g mg^{-1}), associated with surface analysis and activation energy analysis for chemisorption, respectively [38]. The values of α and β can be obtained by plotting q_t vs. ln(t).

Figs. 7a, b, c, and d reveal that the data of kinetic results reasonably matches the pseudo-second-order kinetic model, which has R^2 values of 0.96 and 0.99 for iron and phosphate, respectively. This demonstrates that the number of adsorption sites on the ZnS nanoparticles' surface as well as the concentration of iron and phosphate have an impact on the rate. The kinetic parameters determined using pseudo-first order and pseudo-second order are displayed in **Table 1**.
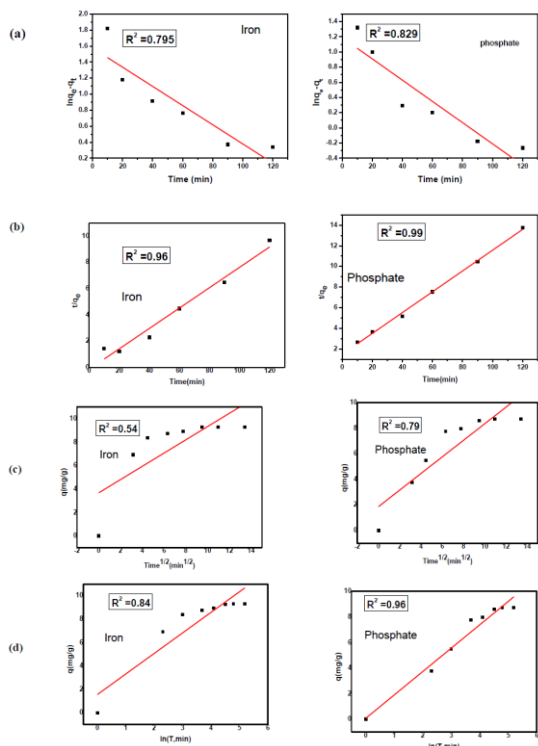

Fig. 7: Adsorption kinetic study of Iron and phosphate on ZnS NPs (a) pseudo-first-order (b) pseudo second- order.(c) intraparticle diffusion and (d) Elovich equations

3.2.2. Adsorption isotherm

The interaction between the adsorbent and adsorbate is well described by the adsorption isotherm. The experimental results were analysed using three nonlinear isotherm models, including the Langmuir, Temkin, and Freundlich isotherms [39, 40]. The Langmuir isotherm model states that adsorption happens as homogenous monolayer adsorption onto a surface with a finite number of uniformly distributed adsorption sites. Adsorbate does not diffuse across the planar adsorbent surface [41].

Equation (7) can be used to express the Langmuir isotherm model in linear form:

Table 1: Kinetics parameter for Iron and phosphate adsorption

Kinetic model	Prameter	Fe^{2+}	PO$_4^{3-}$
Pseudo-first Order	k$_1$ (min^{-1})	8.3×10^{-5}	1×10^{-4}
	R^2	0.79	0.82
	q$_e$	2.4	5.4
Pseudo second-order	k$_2$ (g mg^{-1} min^{-1})	0.02	0.003
	R^2	0.96	0.996
	q$_e$	12.9	10
Intra-particle diffusion	c (mg/g)	7.13	3.62
	R^2	0.63	0.707
	Kp (mg/g·min$^{1/2}$)	0.195	0.46
Elovich equation	α (mg g^{-1} min^{-1})	5.44	1.9
	R^2	0.82	0.88
	β (g/mg)	1.3	0.588

$$\frac{C_e}{q_e} = \frac{1}{q_m}C_e + \frac{1}{K_l q_m} \qquad (7)$$

Where q_e, q_m, C_e, and K_l have the corresponding adsorption capacity (mg/g), maximum adsorption capacity (mg/g), equilibrium concentration (mg/l), and adsorption equilibrium constant called the Langmuir constant (mg/l), respectively [42]. The Freundlich isotherm model predicts that the adsorption is multilayer heterogeneous, and Equation (8) can describe its linear form:

$$\log q_e = \log K_F + \frac{1}{n}\log C_e \qquad (8)$$

where K_F, n, C_e, and q_e are the Freundlich constant (mg/g), a constant, equilibrium concentration (mg/l), and corresponding adsorption capacity (mg/g), respectively. The Temkin isotherm hypothesis for this model states that as the surface area covered by adsorbate and adsorbent interactions increases, the heat of adsorption for the molecules in the layer decreases linearly. This model is represented by Equation (9):

$$q_e = \frac{RT}{b_t} + \ln(k_t C_e) \qquad (9)$$

Here, K_T is the equilibration constant; and b_T is the adsorption heat. Plotting q_e against ln C_e allowed for the calculation of b_T and K_T values for the ions iron and phosphate, adsorption data for the Langmuir, Freundlich, and Temkin isotherm models are presented in **Fig. 8 (a–c)**, respectively. The variables that were calculated using the provided isotherm models are listed in **Table 2**. Based on R^2 values, the Langmuir model is the best isotherm model for the adsorption of iron and phosphate. The adsorption capacities (q_m) of ZnS nanoparticles were compared with different adsorbents The comparison results of five kinds of adsorbents presented in **Table 3** indicate that the iron adsorption capacities of ZSN's were higher than other adsorbents

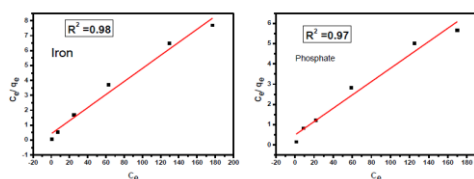while the phosphate adsorption capacities of ZSN's was higher than other adsorbents expect for SA-ZrBT.

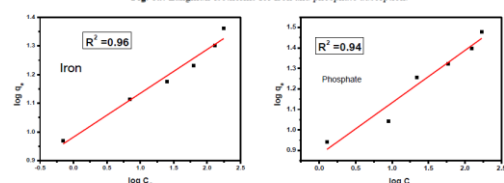**Fig. 8a:** Langmuir isotherms for Iron and phosphate adsorption.

Fig. 8b: Freundlich isotherms for Iron and phosphate adsorption.

Table 2: Isotherm parameters for Iron and phosphate adsorption

Model	Prameter	Fe^{2+}	PO_4^{3-}
Langmuir	Qmax (mg g^{-1})	23.3	31.3
	K_L (L mg^{-1})	0.018	0.015
	R^2	0.98	0.97
Freundlich	Kf (mg g^{-1})	2.66	2.38
	n	6.66	4
	R^2	0.96	0.94
Temkin	K_T (L mg^{-1})	565	3.39
	b_T (J mol^{-1})	2.25	4.2
	R^2	0.88	0.89

Table 3: Comparison of ZnSNPs with other adsorbents for iron and phosphorus adsorption capacity

	Adsorbent	concentration range (mg/L)	Maximum adsorption capacity (mg/g)	References
Iron	HApMn	2-12	0.603	[44]
	CuO Nps	2-10	3.43	[45]
	(GAC)	0-10	14.86	[46]
	(AIR-120H)	0-10	15.6	[46]
	Zns Nps	20-200	23.3	This study
Phosphate	SA-ZrBT	5-100	37.5	[47]
	VPPCC	2-80	1.87	[48]
	WO3 NPs	0-60	19	[49]
	SnO2 NPs	0-60	21.5	[49]
	ZnS NPs	10-200	31.3	This study

3.4 Regeneration study

The regeneration process was followed by the previously published procedure [43]. ZSN's was subjected to an adsorption process at a concentration of 10 mg/L of both iron and phosphate for 120 min. 10 ml of 2M NaOH solution was used to elute (desorbed) the iron and phosphate ions from ZSN's after each adsorption operation. After that, the adsorbent was cleaned to the proper pH using extra-distilled water. The adsorption-desorption cycles were repeated a fifth time. After the fifth cycle, the removal efficiencies for iron ions dropped to 70% and 60% for phosphate ions, respectively.

3.5. Natural Water Sample Treatment

The concentrations of iron and phosphate before and after placing the adsorbent in various samples taken from different wells in El Kharja and surface wells (used for irrigation) are shown in **Table 4**. The data

reveals that under the optimized conditions used in the batch adsorption study, the removal efficiency was 92.2% and 86.5% for iron and phosphate respectively.

Table 4: Iron and phosphate removal efficiency from real samples

	Sample name	Initial concentration (mg/l)	Final concentration (mg/l)	Removal (%)
Iron	Elkharja 16	1.73	0.11	93.6
	Elkharja 55/4	2.3	0.17	92.6
	Elkharja 42	0.89	0.05	94.4
	Elkharja 27	3.91	0.45	88.5
Phosphate	Sample 1	1.41	0.18	87.2
	Sample 2	1.05	0.09	91.4
	Sample 3	1.56	0.2	87.2
	Sample 4	1.27	0.25	80.3

4. Conclusion

This work successfully synthesized ZSN's using the sol-gel process, and it used XRD, IR, UV-Vis DRS, BET, and TEM techniques to describe it. ZSN's were used to remove iron and phosphate from both laboratory-based synthetic water and natural water that was gathered from the El Kharja area. The effects of solution pH, contact time, adsorbent dosage, and starting iron and phosphate content on the adsorption capacity were investigated. Adsorption of iron and phosphate on ZnS (ZSN's) follows the pseudo-second-order kinetic model, Langmuir adsorption isotherm, Adsorption capacity from the Langmuir model is 23.3 and 31.3 mg/g for iron and phosphate, respectively. The study's findings lead to the conclusion that synthesized ZSN's represent a promising possibility for the removal of iron ions from groundwater and phosphate ions from wastewater.

Conflicts of interest

The authors declare that they have no known competing financial interests or personal relationships that could have appeared to influence the work reported in this paper.

References

[1] Hala A. Kiwaan, Farid Sh. Mohamed, Naser A. El-Ghamaz, Nesma M. Beshry, Ashraf A. El-Bindary, Experimental and electrical studies of zeolitic imidazolate framework-8 for the adsorption of different dyes, Journal of Molecular Liquids, Volume 338, 2021, 116670.

[2] Wang, Y., Lin, H., Lin, Z., & Yuan, Y. (2018, July). Application and prospect of talc as heavy

metal passivation agent. In IOP Conference Series: Materials Science and Engineering (Vol. 392, No. 3, p. 032029). IOP Publishing.

[3] García-Mendieta, A., Solache-Ríos, M., & Olguín, M. T. (2009). Evaluation of the sorption properties of a Mexican clinoptilolite-rich tuff for iron, manganese and iron–manganese systems. Microporous and Mesoporous Materials, 118(1-3), 489-495.

[4] Inglezakis, V. J., Doula, M. K., Aggelatou, V., & Zorpas, A. A. (2010). Removal of iron and manganese from underground water by use of natural minerals in batch mode treatment. Desalination and Water Treatment, 18(1-3), 341-346.

[5] Vries, D., Bertelkamp, C., Kegel, F. S., Hofs, B., Dusseldorp, J., Bruins, J. H., ... & Van den Akker, B. (2017). Iron and manganese removal: Recent advances in modelling treatment efficiency by rapid sand filtration. Water Research, 109, 35-45.

[6] Akoto, O., & Adiyiah, J. (2007). Chemical analysis of drinking water from some communities in the Brong Ahafo region. International Journal of Environmental Science & Technology, 4, 211-214.

[7] Conley, D. J., Paerl, H. W., Howarth, R. W., Boesch, D. F., Seitzinger, S. P., Havens, K. E., ... & Likens, G. E. (2009). Controlling eutrophication: nitrogen and phosphorus. Science, 323(5917), 1014-1015.

[8] Zhu, Z., Zeng, H., Zhu, Y., Yang, F., Zhu, H., Qin, H., & Wei, W. (2013). Kinetics and thermodynamic study of phosphate adsorption on the porous biomorph-genetic composite of α-$Fe_2O_3/Fe_3O_4/C$ with eucalyptus wood microstructure. Separation and Purification Technology, 117, 124-130.

[9] Rathod, M., Mody, K., & Basha, S. (2014). Efficient removal of phosphate from aqueous solutions by red seaweed, Kappaphycus alverezii. Journal of Cleaner Production, 84, 484-493.

[10] Acelas, N. Y., Martin, B. D., López, D., & Jefferson, B. (2015). Selective removal of phosphate from wastewater using hydrated metal oxides dispersed within anionic exchange media. Chemosphere, 119, 1353-1360.

[11] Abdennebi, N., Benhabib, K., Goutaudier, C., & Bagane, M. (2017). Removal of aluminium and iron ions from phosphoric acid by precipitation of organo-metallic complex using organophosphorous reagent. Journal of materials and Environmental Sciences, 8(2), 557-1565.

[12] Dubey, S., Banerjee, S., Upadhyay, S. N., & Sharma, Y. C. (2017). Application of common nano-materials for removal of selected metallic species from water and wastewaters: A critical review. Journal of molecular liquids, 240, 656-677.

[13] Hosseini, H., Rezaei, H., Shahbazi, A., & Maghsoodlu, A. (2016). Application of nano-lignocellulose for removal of nickel ions from aqueous solutions. Environmental Resources Research, 4(2), 213-229.

[14] Piuleac, C. G., Sáez, C., Cañizares, P., Curteanu, S., & Rodrigo, M. A. (2012). Hybrid model of a wastewater-treatment electrolytic process. Int. J. Electrochem. Sci, 7, 6289-6301.

[15] Mondal, P., Majumder, C. B., & Mohanty, B. (2008). Effects of adsorbent dose, its particle size and initial arsenic concentration on the removal of arsenic, iron and manganese from simulated ground water by Fe^{3+} impregnated activated carbon. Journal of Hazardous Materials, 150(3), 695-702.

[16] Mishra, S. P., Das, M., & Dash, U. N. (2010). Review on adverse effects of water contaminants like arsenic, fluoride and phosphate and their remediation. Journal of Scientific and Industrial Research ., 69, 249–253.

[17] De-Bashan, L. E., & Bashan, Y. (2004). Recent advances in removing phosphorus from wastewater and its future use as fertilizer (1997–2003). Water research, 38(19), 4222-4246.

[18] Gouider, M., Mlaik, N., Feki, M., & Sayadi, S. (2011). Integrated physicochemical and biological treatment process for fluoride and phosphorus removal from fertilizer plant wastewater. Water environment research, 83(8), 731-738.

[19] Patel, H. (2019). Fixed-bed column adsorption study: a comprehensive review. Applied Water Science, 9(3), 45.

[20] Fu, J., Chen, Z., Wang, M., Liu, S., Zhang, J., Zhang, J., ... & Xu, Q. (2015). Adsorption of methylene blue by a high-efficiency adsorbent (polydopamine microspheres): kinetics, isotherm, thermodynamics and mechanism analysis. Chemical Engineering Journal, 259, 53-61.

[21] Katal, R., Baei, M. S., Rahmati, H. T., & Esfandian, H. (2012). Kinetic, isotherm and thermodynamic study of nitrate adsorption from aqueous solution using modified rice husk. Journal of Industrial and Engineering Chemistry, 18(1), 295-302.

[22] Lalley, J., Han, C., Mohan, G. R., Dionysiou, D. D., Speth, T. F., Garland, J., & Nadagouda, M. N. (2015). Phosphate removal using modified Bayoxide® E33 adsorption media. Environmental Science: Water Research & Technology, 1(1), 96-107.

[23] Amiri, O., Emadi, H., Hosseinpour-Mashkani, S. S. M., Sabet, M., & Rad, M. M. (2014). Simple and surfactant free synthesis and characterization of CdS/ZnS core–shell nanoparticles and their application in the removal of heavy metals from aqueous solution. RSC Advances, 4(21), 10990-10996.

[24] Amiri, O., Hosseinpour-Mashkani, S. M., Rad, M. M., & Abdvali, F. (2014). Sonochemical

synthesis and characterization of CdS/ZnS core–shell nanoparticles and application in removal of heavy metals from aqueous solution. Superlattices and Microstructures, 66, 67-75.

[25] Pala, I. R., & Brock, S. L. (2012). ZnS nanoparticle gels for remediation of Pb2+ and Hg2+ polluted water. ACS applied materials & interfaces, 4(4), 2160-2167.

[26] Tang, W., & Cameron, D. C. (1996). Electroluminescent zinc sulphide devices produced by sol-gel processing. Thin Solid Films, 280(1-2), 221-226.

[27] Biswas, S., Ghoshal, T., Kar, S., Chakrabarti, S., & Chaudhuri, S. (2008). ZnS nanowire arrays: synthesis, optical and field emission properties. Crystal Growth and Design, 8(7), 2171-2176.

[28] Luo, Duan, Ye, M., Zhang, & Li, G. (2008). Poly (ethylene glycol)-mediated synthesis of hollow ZnS microspheres. The Journal of Physical Chemistry C, 112(7), 2349-2352.

[29] Lin, K. B., & Su, Y. H. (2013). Photoluminescence of Cu: ZnS, Ag: ZnS, and Au: ZnS nanoparticles applied in Bio-LED. Applied Physics B, 113, 351-359.

[30] Zhang, Y., & Yu, M. (2014). One pot synthesis and characterization of ZnS nanoparticles in the mixed surfactant system. Materials Chemistry and Physics, 145(1-2), 197-202.

[31] Farooqi, M. M. H., & Srivastava, R. K. (2014). Structural, optical and photoconductivity study of ZnS nanoparticles synthesized by a low temperature solid state reaction method. Materials science in semiconductor processing, 20, 61-67.

[32] Mahpishanian, S., Sereshti, H., & Baghdadi, M. (2015). Superparamagnetic core–shells anchored onto graphene oxide grafted with phenylethyl amine as a nano-adsorbent for extraction and enrichment of organophosphorus pesticides from fruit, vegetable and water samples. Journal of Chromatography A, 1406, 48-58.

[33] Kamboh, M. A., Ibrahim, W. A. W., Nodeh, H. R., Sanagi, M. M., & Sherazi, S. T. H. (2016). The removal of organophosphorus pesticides from water using a new amino-substituted calixarene-based magnetic sporopollenin. New Journal of Chemistry, 40(4), 3130-3138.

[34] Khoshhesab, Z. M., Ayazi, Z., & Farrokhrouz, Z. (2016). Ultrasound-assisted mixed hemimicelle magnetic solid phase extraction followed by high performance liquid chromatography for the quantification of atorvastatin in biological and aquatic samples. Analytical Methods, 8(24), 4934-4940.

[35] Gupta, V. K., Agarwal, S., Sadegh, H., Ali, G. A., Bharti, A. K., & Makhlouf, A. S. H. (2017). Facile route synthesis of novel graphene oxide-β-cyclodextrin nanocomposite and its application as adsorbent for removal of toxic bisphenol A from the aqueous phase. Journal of Molecular Liquids, 237, 466-472.

[36] Azizian, S. (2004). Kinetic models of sorption: a theoretical analysis. Journal of colloid and Interface Science, 276(1), 47-52.

[37] Singha, B., & Das, S. K. (2013). Adsorptive removal of Cu (II) from aqueous solution and industrial effluent using natural/agricultural wastes. Colloids and Surfaces B: Biointerfaces, 107, 97-106.

[38] Chen, S., Zhang, J., Zhang, C., Yue, Q., Li, Y., & Li, C. (2010). Equilibrium and kinetic studies of methyl orange and methyl violet adsorption on activated carbon derived from Phragmites australis. Desalination, 252(1-3), 149-156.

[39] Verma, R., Asthana, A., Singh, A. K., & Prasad, S. (2017). An arginine functionalized magnetic nano-sorbent for simultaneous removal of three metal ions from water samples. RSC advances, 7(81), 51079-51089.

[40] Panda, L., Rath, S. S., Rao, D. S., Nayak, B. B., Das, B., & Misra, P. K. (2018). Thorough understanding of the kinetics and mechanism of heavy metal adsorption onto a pyrophyllite mine waste based geopolymer. Journal of Molecular Liquids, 263, 428-441.

[41] Hameed, B. H., Din, A. M., & Ahmad, A. L. (2007). Adsorption of methylene blue onto bamboo-based activated carbon: kinetics and equilibrium studies. Journal of hazardous materials, 141(3), 819-825.

[42] He, J., Zhang, K., Wu, S., Cai, X., Chen, K., Li, Y., & Liu, J. (2016). Performance of novel hydroxyapatite nanowires in treatment of fluoride contaminated water. Journal of hazardous materials, 303, 119-130.

[43] Nodeh, H. R., Sereshti, H., Afsharian, E. Z., & Nouri, N. (2017). Enhanced removal of phosphate and nitrate ions from aqueous media using nanosized lanthanum hydrous doped on magnetic graphene nanocomposite. Journal of environmental management, 197, 265-274

[44] Ayash, M. A. E. A. A., Elnasr, T. A. S., & Soliman, M. H. (2019). Removing iron ions contaminants from groundwater using modified nano-hydroxyapatite by nano manganese oxide. Journal of Water Resource and Protection, 11(06), 789.

[45] Chakrabarty, S., Mahmud, M. A., Ara, M. H., & Bhattacharjee, S. (2021). Development of a platform for removal of Iron (III) ions from aqueous solution using CuO nanoparticles. Journal of Water and Environmental Nanotechnology, 6(1), 41-48.

[46] Goher, M. E., Hassan, A. M., Abdel-Moniem, I. A., Fahmy, A. H., Abdo, M. H., & El-

sayed, S. M. (2015). Removal of aluminum, iron and manganese ions from industrial wastes using granular activated carbon and Amberlite IR-120H. The Egyptian Journal of Aquatic Research, 41(2), 155-164.

[47] Xi, H., Li, Q., Yang, Y., Zhang, J., Guo, F., Wang, X., ... & Ruan, S. (2021). Highly effective removal of phosphate from complex water environment with porous Zr-bentonite alginate hydrogel beads: Facile synthesis and adsorption behavior study. Applied Clay Science, 201, 105919.

[48] Darshana Senarathna, D. D. T. T., Namal Abeysooriya, K. H. D., Dunuweera, S. P., Ekanayake, B. P. K., Wijenayake, W. M. H. K., & Rajapakse, R. M. G. (2020). Removal of phosphate from aqueous solutions using chemically synthesized vaterite polymorph of porous calcium carbonate nanoparticles under optimized conditions. Journal of Nanomaterials, 2020, 1-15.

[49] Mahdavi, S., Hassani, A., & Merrikhpour, H. (2020). Aqueous phosphorous adsorption onto SnO2 and WO3 nanoparticles in batch mode: kinetic, isotherm and thermodynamic study. Journal of Experimental Nanoscience, 15(1), 242-265.